Meteorology and Atmospheric Physics (2019) 131:1529–1548
https://doi.org/10.1007/s00703-019-0656-3

ORIGINAL PAPER

Evaluation of WRF planetary boundary layer parameterization schemes for simulation of monsoon depressions over India

Deepika Rai[1] · **Sandeep Pattnaik**[1]

Received: 19 June 2018 / Accepted: 5 January 2019 / Published online: 14 January 2019

Abstract
This study evaluates the fidelity of five planetary boundary layer (PBL) parameterization schemes in the advanced weather research and forecasting model for simulating monsoon depressions (MDs) over India. Five PBL schemes include; nonlocal first-order medium-range forecasting (MRF) and Yonsei University (YSU); hybrid first-order Asymmetric Convective Model version 2 (ACM2), and local one-and-a-half-order Bougeault–Lacarrére (BouLac) and Mellor–Yamada–Nakanishi–Niino (MYNN2). PBL schemes show significant impact on rainfall along with dynamical and thermodynamical parameters associated with MDs at the surface as well as at the upper levels. MRF simulates a relatively shallower, warmer and drier boundary layer compared to others. Results reveal that strong upper-level divergence and high moisture content within the lower levels are favorable for the occurrence of heavy rain associated with MDs. However, stronger wind shear within the mid-troposphere weakens the system and reduces the rain intensity. Based on the results and keeping the rainfall product in view, it is found that nonlocal PBL schemes (MRF and ACM2) have better forecast skills score than local PBL schemes (BouLac and MYNN2) over the Indian region.

1 Introduction

Indian economy, substantially dependent on the agriculture sector, is highly influenced by the distribution of rainfall during the summer monsoon season. The northern tip, northeast, and southeast peninsula of India receives a substantial amount of rainfall during winter, pre-monsoon and post-monsoon seasons, respectively (Deshpande et al. 2012). However, southwest monsoon is an important water source. A large part of the country receives 75–80% of the annual rainfall during the summer monsoon season (Deshpande et al. 2012). Monsoon depressions (MDs) associated with the Indian summer monsoon season brings a significant amount of rainfall and modulate the rainfall distribution over the Indian region. MDs also bring copious rainfall situations causing flash floods and cloudburst situations leading to enormous loss of lives and properties (Rajesh et al. 2016; Dimri et al. 2017). Accurate prediction of rainfall from these intense convective systems is challenging (Krishnamurti et al. 2007). Previous studies, focused on structural features and movement of MDs, were mainly based on the observations (i.e., satellites and in situ measurements) and reanalysis data (Sikka 1977; Goswami 1987; Krishnamurthy and Ajayamohan 2010; Hunt et al. 2016; Fletcher et al. 2018). As MDs play a dominant role in modulating monsoon rainfall and associated damages, evaluation of these systems in operational and research numerical weather prediction modeling systems such as weather research and forecasting (WRF) model is of critical importance.

An appreciable sensitivity of planetary boundary layer (PBL) parameterizations are shown in simulating different weather conditions over various regions, e.g., severe cold season weather conditions at southeastern United States (Cohen et al. 2015), diurnal cycles of surface winds and temperatures over the central United States (Zhang and Zheng 2004), boundary layer variable over complex orographic area in southern Italy (Avolio et al. 2017), etc. Some recent studies compared different PBL parameterizations over different tropical sites (Hariprasad et al. 2014) and climatic

Responsible Editor: S. Trini Castelli.

Electronic supplementary material The online version of this article (https://doi.org/10.1007/s00703-019-0656-3) contains supplementary material, which is available to authorized users.

✉ Sandeep Pattnaik
spt@iitbbs.ac.in

[1] School of Earth Ocean and Climate Sciences, Indian Institute of Technology Bhubaneswar, Argul, Jatni, Khordha, Bhubaneswar, Odisha 752050, India

zones (Gunwani and Mohan 2017) over India. Earlier studies demonstrated that PBL parameterization directly affects the vertical mixing and modulate the mixed layer depth and the associated moisture availability over Indian region (Sathyanadh et al. 2017a).

A number of research works are published to understand the sensitivity of heavy rainfall events to the PBL parameterizations. PBL parameterization directly affects the vertical mixing and modulate the mixed layer depth along with associated moisture availability over the Indian region (Sathyanadh et al. 2017a). The intensity of convective systems depends on the exchange of surface energy, as moisture and heat, between the surface and upper layers through vertical mixing. High vertical mixing transports more moisture from the surface to the free atmosphere, and hence favors the precipitation associated with heavy rainfall events (Wisse and Arellano 2004). In contrast, weak vertical mixing confines the moisture to lower levels, which in turn, decreases the condensates and corresponding latent heating, and hence reduces the surface precipitation (Efstathiou et al. 2013). Vertical mixing processes differ between local and non-local mixing. Comparing local and non-local diffusion approaches, Hong and Pan (1996) showed that non-local approach substantially improves the precipitation forecast by enhancing the convective overturning. The rainfall forecasts are more sensitive to the PBL and microphysics than the land surface models (Singh et al. 2018). Further, using Weather Research and Forecasting (WRF) model for the simulation of an extremely heavy rainfall event over Chennai, Srinivas et al. (2018) showed the impact of PBL parameterizations in the prediction of rainfall by modulating the location of upper air circulation, energy transport, moisture convergence and intensity of convection.

In comparison to other weather events, very few studies are undertaken to examine the impact of different PBL parameterizations on MDs. Using WRF, Flaounas et al. (2011) demonstrated a strong sensitivity of the vertical distribution of temperature and relative humidity and rainfall amounts associated with the West African summer monsoon season to PBL schemes. Cha et al. (2008) and ZiQian et al. (2014) showed that an excessive PBL mixing results as positive feedback between convective precipitation and surface latent heat flux (LHF) over the ocean during the East Asian Summer monsoon. Using reanalysis data, Patil et al. (2013) and Sathyanadh et al. (2017b) showed the variations in the PBL height (PBLH) during pre-monsoon, monsoon, and post-monsoon seasons along with excess and deficit monsoon years over India. Patil et al. (2013) concluded that during excess (deficient) monsoon years, strong (weak) convection and low-level jets are associated with deep (shallow) PBLH over north-west India (Patil et al. 2013). PBLHs are shallow/deep during active/break monsoon periods over central India (Sathyanadh et al. 2017b) and southern Peninsular India (Sandeep et al. 2014).

Although PBL parameterizations show significant impact in the forecast of rainfall during summer monsoon seasons, limited studies are available over the Indian region. Potty et al. (1997) and Basu et al. (1999) compared different local PBL schemes following different mixing criteria. For one scheme, vertical mixing was a function of wind shear, whereas for other it was defined in term of turbulent kinetic energy (TKE). They suggested that TKE-based scheme performed better MD track and monsoon circulation over the Indian subcontinent. Further, using National Center for Medium-Range Weather Forecasting general circulation model, Basu et al. (2002) compared the role of two PBL parameterizations (local and non-local) for simulation of MDs and suggested that incorporation of non-local closure improves the forecast of precipitation and flow pattern associated with MDs over the Indian region. The results suggest a substantial sensitivity of PBL parameterizations to the convective rain-bearing systems, however, studies are mostly based on either general circulation model (Hong and Pan 1996; Basu et al. 2002) or seasonal forecast (Basu et al. 1999; Cha et al. 2008; Flaounas et al. 2011; ZiQian et al. 2014). Further, recent studies have demonstrated that the increase in horizontal resolution of numerical models improves the forecast skills at different scales, e.g., mesoscale (Bryan and Morrison 2012), synoptic (Hill and Lackmann 2009; Strachan et al. 2013; Hunt and Turner 2017), and global (Roeckner et al. 2006) scales. However, in past literature, sensitivity experiments were carried out at a coarser resolution, i.e., >50 km (Potty et al. 1997; Basu et al. 1999, 2002).

In a nutshell, MDs are highly relevant to the Indian monsoon system and rainfall with critical socio-economic relevance. However, limited investigations were carried out to comprehensively quantify and characterize its sensitivity to the PBL parameterization in a numerical model such as WRF, which is extensively used in many operational and research agencies across the globe including Indian Meteorological Department (IMD). In addition, literature quantifying the responses of MDs to the PBL parameterization particularly over the land region is not available. Therefore, this study is primarily focused on assessing the impact of different PBL schemes on rainfall and important dynamic and thermodynamic characteristics of MDs at the surface as well as at the upper level with a lead time up to 72 h. Moreover, duration of simulation is considered with the special emphasis on the existence MDs over the Indian landmass. The layout for the remaining paper is; model and methodology in Sect. 2, a brief description of the PBL schemes in Sect. 3, result and discussions in Sect. 4, and the summary in Sect. 5.

2 Model and methodology

2.1 Case description

Three MDs (a) JUL14 (0000 UTC 21—0000 UTC 24 July 2014), (b) AUG14 (1200 UTC 04—1200 UTC 07 August 2014), and (c) JUL15 (0000 UTC 27—0000 UTC 30 July 2015) considered for this study are selected broadly under following criteria; MDs (a) must have notable initial propagation, (b) have at least 48 h of its life cycle over land region, (c) rainfall > 35.5 mm day^{-1} measured at station, classified as heavy rain as per IMD (http://imd.gov.in/section/nhac/wxfaq.pdf). Detailed description about JUL14 and JUL15 are given in Table S1, with a brief description about AUG14 as follows.

2.1.1 August14 (1200 UTC 4 August – 0000 UTC 7 August 2014)

A depression, formed over the north Bay of Bengal (BoB) off the West Bengal coast on 1200 UTC 3 August, moved west-northwestwards and intensified into a deep depression at 21.9°N and 88.3°E on 1800 UTC 3 August 2014. The system, as a deep depression till 0600 UTC 5 August, weakened into a depression at 23.5°N and 82.5°E on 0900 UTC 5 August 2014. Further moving west-northwestward (Fig. 1b), it weakened into a low-pressure area over northwest Madhya Pradesh on 0300 UTC 7 August 2014 and merged with the monsoon trough on 8 August 2014. This deep depression resulted in torrential rains and flood which caused 47 human causalities, 149 livestock loss, and 45,953 house damage, along with 3,67,692 hectare of affected crop area in Odisha. IMD (2015) gives a detailed description of this system. Keeping the severity of the storm, this case has been discussed in depth.

2.2 Model and experiments design

Advanced Weather Research and Forecasting (WRF–ARW) model version 3.6 (Skamarock et al. 2008) is used to carry out sensitivity experiments. The model configuration consists of two-way interactive triply nested domains with the model top set at 50 hPa. Table 1 depicts the detailed model configurations and data used for comparison of the model outcomes. Except for PBL schemes, other model configurations are identical. The five PBL schemes used are Medium-Range Forecasting (MRF), Yonsei University (YSU), Asymmetric Convective Model version 2 (ACM2), Bougeault–Lacarrére (BouLac), and Mellor–Yamada–Nakanishi–Niino (MYNN2). In the following sections, experiments using YSU, MRF, ACM2, MYNN2, and BouLac schemes are referred to as YSU, MRF, ACM2, MYNN2, and BouLac, respectively. All results discussed are from the inner domain, i.e., 3-km resolution.

The global precipitation measurement (GPM) data are used to validate the model rainfall. GPM level 3 merged products have 0.1° × 0.1° horizontal resolution and 30-min temporal resolution (Hou et al. 2014). The design of the GPM core observatory is an advancement of tropical rainfall measuring mission's (TRMM's) rain-sensing package, which used an active radar capable of providing information on precipitation particles, layer-by-layer, within clouds, and a passive microwave imager capable of sensing the total precipitation within all cloud layers. Since light rain and falling snow account for a significant fraction of precipitation occurrence in middle and high latitudes, GPM instruments extend the capabilities of TRMM sensors to detect falling snow, measure light rain, and provide quantitative estimates of microphysical properties of precipitation particles.

The fifth generation of European Centre for Medium-Range Weather Forecasting (ECMWF) Reanalysis (ERA5) data sets are used for comparison of surface properties along with the vertical structure of MDs. ERA5, a global climate reanalysis data, is being developed through the Copernicus

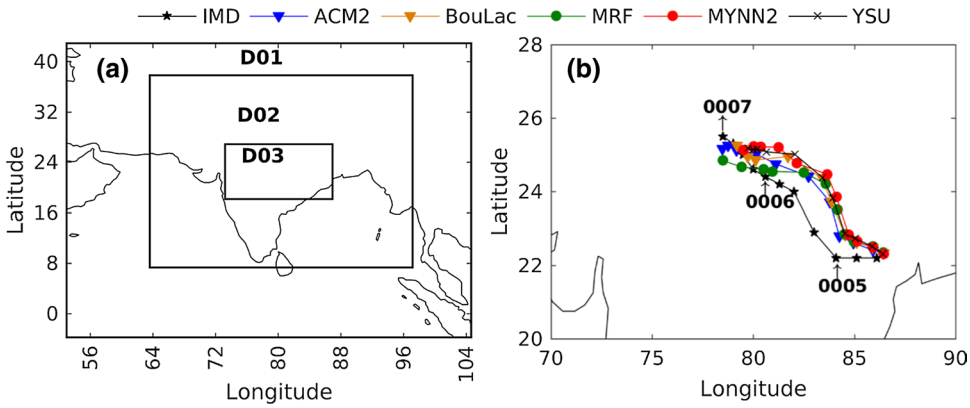

Fig. 1 **a** Modeling domains used in WRF-ARW (D01—27 km resolution; D02—9 km resolution; and D03–3 km resolution and **b** track for AUG14. Here 4-digits numbers along the tracks represent the time (in UTC) and date

Table 1 Summary of the model configuration and data used for model validation

	D01/D02/D03
Simulation duration	1200 UTC 04–1200 UTC 07 August, 2014
Horizontal resolution (km)	27/9/3
Grid points (east–west, north–south)	278 × 250; 387 × 387; 474 × 327
Vertical levels	35
Initial condition	3 hourly Global Forecast System (GFS) data with 0.5° × 0.5° horizontal resolutions
Physics schemes	
Cumulus	Kain–Fritsch (Kain, 2004) (only for D01 and D02)
Microphysics	WRF Single Moment 6-class (Hong and Lim 2006)
Land surface	Unified Noah land-surface model (Ek et al. 2003)
Surface layer	Revised MM5 Monin–Obukhov surface layer scheme (Jimenez et al. 2012)
Shortwave	Dudhia (Dudhia 1989)
Longwave	Rapid Radiative Transfer Model (Mlawer et al. 1997)
Shallow cumulus	Global/Regional Integrated Model system (Hong et al. 2013)
Data for comparison of model output	
Track rainfall	6 hourly best track data from Indian Meteorological Department (IMD) 30 min Global Precipitation Measurement (GPM) data with 0.1° × 0.1° horizontal resolutions
2 m temperature; 10 m wind speed; vertical profiles of temperature, wind speed, specific and relative humidity	Fifth generation European Centre for Medium-Range Weather Forecasting (ECMWF) ReAnalysis (ERA5) data with hourly and ~ 31 km temporal and horizontal resolutions, respectively

Climate Change Service. It was released in July 2017 and is a successor of ERA-Interim. These data cover the Earth on a ~ 31-km grid resolution on an hourly basis and resolve the atmosphere using 137 levels from the surface to the height up to 80 km. Details about the ERA5 data are available at the ECMWF online link (https://software.ecmwf.int/wiki/display/CKB/ERA5+data+documentation). GPM and ERA5 data are interpolated to match with the simulation domain and resolution for the statistical calculation, whereas, are used directly with a fixed domain as for simulation for spatial and domain averaged plots.

The domain of simulation and the propagation of AUG14 are shown in Fig. 1, whereas for JUL14 and JUL15 in supporting information (Figs. S1–S2). The tracks are shown for the period when the storm was either in a depression or deep depression phase. Experiments reproduce the storm track with a substantial deviation compared to IMD. Simulated tracks are relatively northeastward compared to IMD (Fig. 1b). Further, MRF shows a relatively faster movement and more close to IMD track than other experiments.

3 Description of PBL schemes

The PBL schemes adopt different assumptions regarding the transport of moisture, mass, and energy within the atmosphere. Vertical mixing strength, entrainment flux, PBLH, vertical eddy diffusivity, etc. affect the above-mentioned transports and are formulated differently in different PBL schemes. The five PBL schemes used here follow two different approaches of turbulence closure known as local (i.e., MYNN2 and BouLac) and non-local (i.e., MRF, ACM2, and YSU). YSU, MRF, and ACM2 are the first-order closure schemes, follow non-local diffusion within the PBL and local diffusion above. These schemes are based on nonlocal K-theory within the PBL. K-theory follows a specific profile of eddy diffusivity coefficient which is a function of PBLH, surface friction velocity, and stability. Above the PBL, eddy diffusivity coefficient is a function of local wind shear and local Richardson number. Following are some of the important features of these schemes.

The YSU scheme (Hong et al. 2006) is a revised version of MRF schemes (Hong and Pan 1996). It includes an explicit treatment of entrainment processes at the top of the PBL which is absent in MRF. The PBL height for YSU under convective/stable conditions is defined as the level where the surface simulated bulk Richardson number exceeds a critical threshold (0/0.25). The PBLH for MRF is also based on bulk Richardson number, but in this case, threshold is defined as 0.5. Observations suggest that, only when Richardson number is less than 0.25, the mechanical production is intense enough to sustain turbulence in a stable layer (Holton 2004). The increase in critical Richardson number enhances the vertical mixing in the stable boundary layer and hence the PBL height.

ACM2 is the first-order, K-theory-based hybrid (combination of nonlocal and local) scheme (Pleim 2007a, b). For any prognostic mean variables at a given level, ACM2

explicitly contains nonlocal upward fluxes from the surface and downward fluxes from (to) the adjacent upper (lower) vertical level within the boundary layer. This scheme treats nonlocal fluxes using a transilient term. PBLH in ACM2 is diagnosed as the level where bulk Richardson number is equal to 0.25.

Higher-order closures are proposed for more realistic transport of surface fluxes under strongly unstable conditions and to overcome the deficiencies of unrealistic near surface adiabatic layers under strong heating conditions. MYNN2 (Nakanishi and Niino 2004, 2009) and BouLac (Bougeault and Lacarrere 1989) are 1.5-order local closure schemes which require an additional prognostic equation of the turbulent kinetic energy (TKE) and also known as TKE closure scheme. In both these schemes, the eddy diffusivity coefficients for momentum and heat are parameterized through the use of turbulent kinetic energy (TKE), mixing length, and stability and are independent of PBLH. TKE closure schemes differ in terms of the calculation of stability and mixing length. Another difference between the BouLac and MYNN2 is the presence of a counter-gradient term in the parameterization of heat flux for BouLac in the convective conditions. This counter-gradient correction in BouLac allows for slightly stable stratification persisting with upward heat flux. PBLH for TKE closure scheme is defined as the height where prognostic TKE is sufficiently small (of the order of 0.005 m^2 s^{-2}).

4 Results and discussions

4.1 Movement of the system

Figure 1b compares the track of MDs with IMD best track data. The simulated tracks are based on the streamline at 850 hPa and shown for the period when the system was either a depression or deep depression. Experiments are able to reproduce the northwestward progress of the system with about 70 km northward deviation from IMD during 0000 UTC 5 August–0000 UTC 6 August 2014 (Fig. 1b). Overall, the simulated tracks show a rightward shift with respect to the IMD track. Similar to AUG14, simulations for JUL14 and JUL15 could replicate the track with a rightward shift with respect to IMD (Fig. S2).

4.2 Rainfall

Rainfall is one of the most important features of the MDs. Figure 2 shows the time series of domain-averaged rain rate for the experiments and compares with GPM. Experiments produce the highest rain > 24 mm day^{-1} during 1800 UTC 4 August to 0000 UTC 5 August, following a decrease in rain rate with some rain peaks during 1500 UTC 5 August–0000 UTC 6 August, and 0600–1200 UTC 6 August. Rain rate is less than 5 mm day^{-1} from 2100 UTC 6 August onwards. The model shows a close resemblance with GPM during 1800 UTC 4 August–0000 UTC 5 August and 2100 UTC 6 August–1200 UTC 7 August and underestimates for rest of the times. Overall, BouLac and MRF show the maximum (3–27 mm day^{-1}) and minimum (2–25 mm day^{-1}) rain rate than others for most of the simulation duration.

The domain-averaged rain rate (Fig. 2) shows that WRF simulations are unable to capture the rainfall peaks particularly during 1200 UTC 5 August–1200 UTC 6 August 2014. This deficiency is due to a higher number of grid points (10–20%) associated with low rainfall (< 10 mm day^{-1}) in model forecast compared to observations (Fig. 3). A large number of grid points associated with lower rain rate leads to an overall reduction of domain–averaged rain rate, hence missing the peaks (Fig. 2). BouLac, MYNN2, and YSU simulate relatively better precipitation particularly at lower range (< 35.5 mm day^{-1}) than ACM2 and MRF in terms of grid points (Fig. 3). Figure 4 indicates that experiments could capture the heavy rain pocket associated with AUG14 but differ in spatial extent during 1200 UTC 5 August–1200 UTC 6 August 2014. The rainfall magnitude > 35.5 mm day^{-1} for MRF could reach up to 76°E, whereas mostly east of 78°E for others. Further, the spatial distribution of rainfall < 35.5 mm day^{-1} are better captured by MRF and ACM2 than others. Except for MRF, other

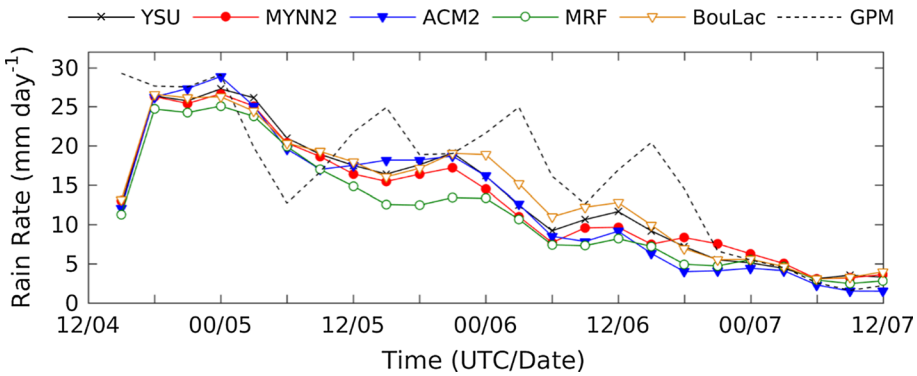

Fig. 2 Time-series of rain rate (mm day^{-1}) at 3 h interval. The model outputs are compared with the GPM rainfall data. Here, four digits along abscissa the UTC time and date, respectively

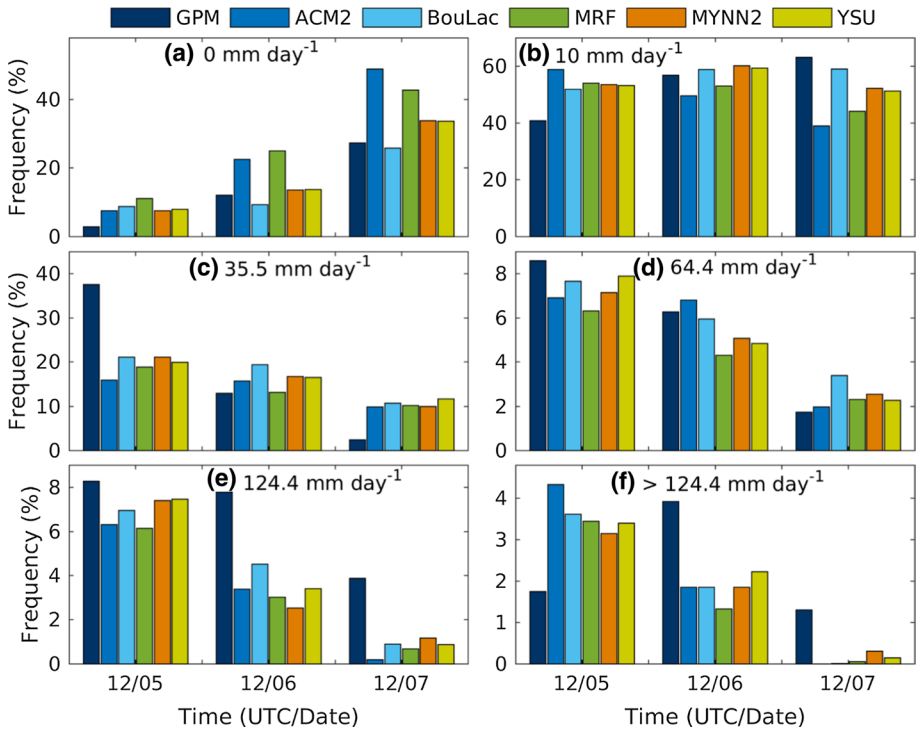

Fig. 3 Frequency distribution of daily rainfall for AUG14 with time for rainfall at different thresholds. Daily rainfall data from GPM is used to validate the model simulated rainfall

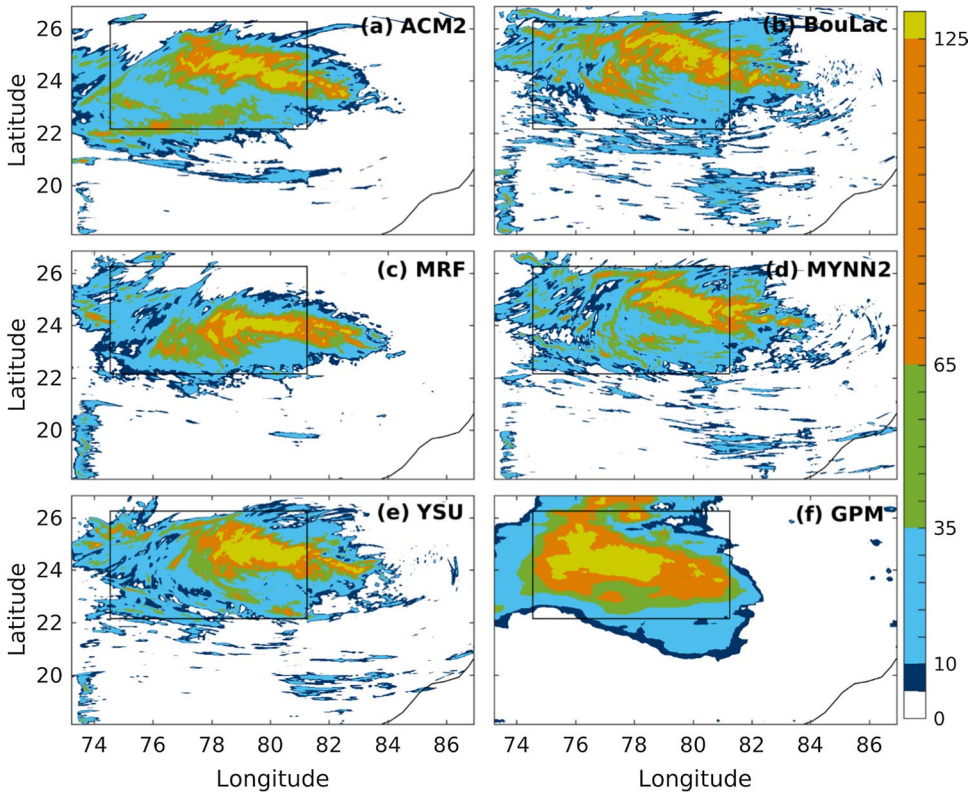

Fig. 4 Spatial distribution of accumulated rainfall (mm day^{-1}) for AUG14 during 1200 UTC 5–6 August 2014. The box within the domain shows the area associated with the major rain during this period

experiments show a relatively more northeastward movement than GPM (Figs. 4, 5). These results are very similar to other cases, i.e., JUL14 and JUL15 (Figs. S4, S5).

Since a considerable movement of the system is found along the longitude (Fig. 1b), longitude–time cross sections of rain rate over the domain of simulation are compared

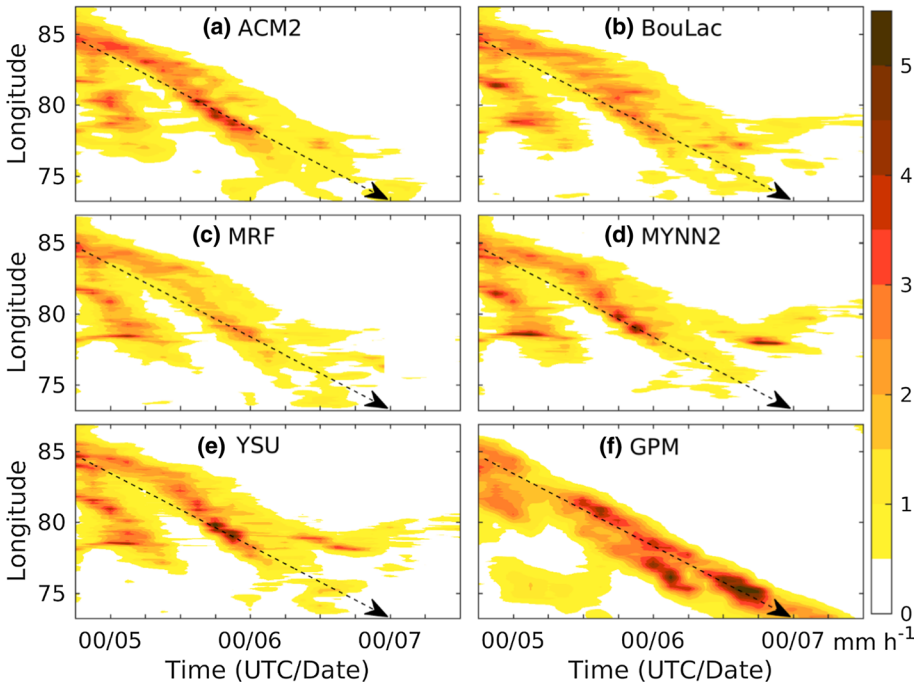

Fig. 5 Longitude-time cross-sections of rain rate (mm h^{-1}) over the domain of simulation for **a** ACM2, **b** BouLac, **c** MRF, **d** MYNN2, **e** YSU, and **f** GPM. The arrow represents the progress of the maximum rain rate for GPM

with GPM (Fig. 5). It is found that experiments are able to replicate the GPM rain rate up to 0600 UTC 5 August and underestimate afterward. Experiments could not reproduce the rain rate greater than 4 mm h^{-1} for GPM after 0000 UTC 6 August. The experiments show the presence of a rain patch about 2 mm h^{-1} between 78°E and 80°E from 0600 UTC 6 August onwards, except ACM2 and MRF. Results suggest that PBL schemes affect the magnitude and spatial distribution of rainfall associated with MDs. As the experimental setup is identical, except PBL, for all the experiments, the results are primarily attributed to the responses of PBL parameterization. However, being highly non-linear systems, the responses of different PBL to model resolution, cumulus parameterizations, and microphysics might not be completely discarded.

To further investigate the sensitivity of the rainfall characteristics to the PBL parameterizations, few statistical analysis, namely Equitable Threat Score (ETS), Critical Success Index (CSI), False Alarm Rate (FAR), Heidke Skill Score (HSS), Probability of Detection (POD), and Percent Correct (PC) are discussed. These statistics (Appendix 1) are calculated against GPM data.

Figure 6 compares ETS over daily rainfall. In general, ETS decreases with increasing thresholds. At day 1 (i.e., 1200 UTC 4 August–1200 UTC 5 August), maximum ETS reached up to 0.23 at 20 mm, i.e., light rain threshold (MYNN2) and decreased below 0.03 at 200 mm threshold (Fig. 6a). MRF shows the highest ETS reaching up to 0.22 followed by ACM2 and BouLac is associated with the lowest ETS for all the thresholds (Fig. 6a). At day 2 (1200 UTC 5 August–1200 UTC 6 August), ETS for experiments shows a continuous decrease from 0.43 to almost zero (Fig. 6b). MRF and ACM2 show higher ETS than others at all the thresholds. The highest ETS for ACM2/MRF is 0.43/0.40 at 20/10 mm threshold, whereas MYNN2 is associated with the lowest ETS, followed by BouLac at all the thresholds (Fig. 6b). At day 3 (i.e., 1200 UTC 6 August–1200 UTC 7 August), ETS is reduced to 0.16 with the highest ETS for MRF and is restricted below 90 mm day^{-1} thresholds. ETS is mostly negative for MYNN2 at day 3 (Fig. 6c).

Like ETS, CSI also shows a decrease with the thresholds and a better skill for MRF than others (Table 2). At day 1, MYNN2 and YSU show a slightly higher CSI for rain less than 30 mm. Above 30 mm threshold, MRF shows the highest values followed by ACM2 than others and BouLac presents the lowest CSI for all the thresholds at day 1. At day 2, CSI is relatively higher than day 1 for thresholds less than 30 mm. The highest CSI values are associated with ACM2 and MRF emerges as the second best among all. MYNN2 is associated with the lowest CSI, followed by BouLac at day 2. At day 3, CSI is the highest/lowest for MRF/MYNN2 and is limited within thresholds less than 90 mm. Results suggest that MRF gives a better ETS and CSI for thresholds > 30 mm at day 1 and day 2. For day 3, ETS and CSI are the best for MRF at all thresholds. Usually, for any simulation, model needs a spin-up time which depends upon initial condition, data assimilation, model configuration, integration, etc. This spin-up time is responsible for the higher ETS and CSI at day 2 than day 1. Similarly, FAR, HSS, PC, and POD also indicate that MRF is the best scheme in terms of rain skills and ACM2 emerges as the second-best scheme than others (Table 2). Rain skills are relatively poor for local schemes,

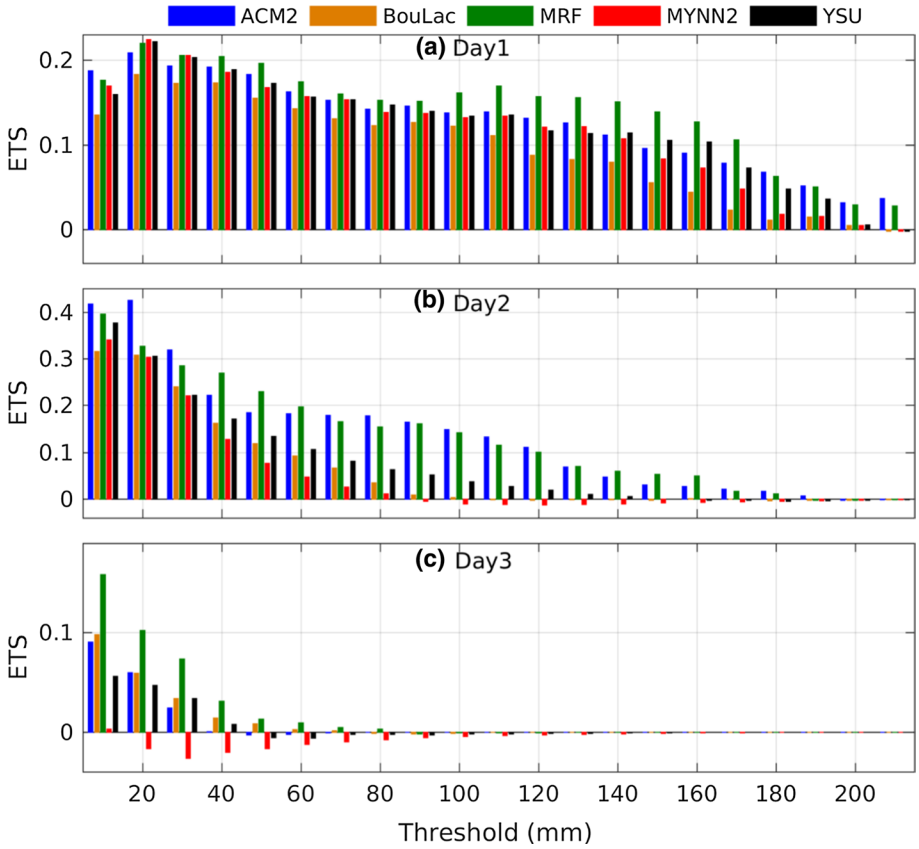

Fig. 6 Equitable threat score (ETS) of daily rainfall. GPM data is used to validate the model simulated rainfall

e.g., MYNN2 and BouLac (Table 2). Overall, MRF shows a better forecast of rainfall associated with the MD and ACM2 represents the second-best scheme among all. Similar results are shown for JUL14 and JUL15 (Tables S2, S3).

4.3 Surface and PBL parameters

Figure 7a, b compares the model 10 m wind speed (WS_{10m}) and 2 m temperature (T_{2m}) with ERA5. It is found that the variations in simulated variables are similar, however, stronger than ERA5. WS_{10m} shows the highest peak above 6.5 m s^{-1} during 0300 UTC–0900 UTC and lowest peak during night time between 1500 UTC and 0000 UTC (Fig. 7a). Experiments overestimate WS_{10m}; however, MRF is able to represent it better than others particularly during the nighttime (Fig. 7a). BouLac simulates the strongest WS_{10m} (> 5 m s^{-1}) during the night (1500 UTC–0000 UTC) and overestimate it about 1 m s^{-1} compared to ERA5. MYNN2 and YSU simulate the strongest WS_{10m} (> 6 m s^{-1}) during the daytime (0300 UTC–1200 UTC) (Fig. 7a). Variation in WS_{10m} for ACM2 is similar to MRF for most of the times.

Time series of T_{2m} shows diurnal variations with a maximum at 0900 UTC, i.e., local afternoon, which is increasing from 303 to 304 K with time (Fig. 7b). Experiments overestimate T_{2m} with roughly more than 1 K than ERA5 during the daytime (0300 UTC–1500 UTC). ACM2 shows the minimum deviation from ERA5 (~ 1 K) and MRF is closer to ACM2 than others (Fig. 7b). Inter-comparison among the experiments show that T_{2m} do not vary much during night time, but the variations are substantial during the daytime. It is noted that as the rain rate decreases (Fig. 2), the temperature variations among experiments also decreases (Fig. 7b). The maximum deviation among the experiments is about 1 K at 0900 UTC 5 August, which is reduced to 0.5 K at 0900 UTC 7 August. Further, YSU, MYNN2, and BouLac show coherent variations throughout the simulation duration.

In Tables 3 and 4, model performance has been evaluated using standard statistical measures such as Index of Agreement (IOA), Bias, Fractional Bias (FB), and Root Mean Square Error (RMSE) discussed in Appendix 2. According to Emery et al. (2001), the statistical benchmark for meteorological parameter temperature (wind speed) is IOA > 0.7 (0.6); bias ± 0.5 K (0.5 m s^{-1}); and RMSE 2 K (2 m s^{-1}).

Table 3 shows the statistics of T_{2m} for different experiments, e.g., JUL14, AUG14, and JUL15. All simulations, except AUG14, show low IOA magnitudes than acceptable range (> 0.7 K). Bias generally lie on the higher side of the acceptable range (bias < 0.5 K) and FB lie on the lower side of the acceptable range (FB < 0.5). As discussed earlier in Fig. 7b, experiments overestimate the surface temperature (negative FB). In terms of statistics, ACM2 shows the best performance of T_{2m} as shown in Fig. 7b also.

Table 2 Critical Success Index (CSI), false alarm rate (FAR), Heidke Skill Score (HSS), percent correct (PC), and probability of detection (POD) at different thresholds

Threshold	20 (mm day^{-1}) day 1/day 2/day 3	60 (mm day^{-1}) day 1/day 2/day 3	100 (mm day^{-1}) day 1/day 2/day 3	140 (mm day^{-1}) day 1/day 2/day 3
CSI				
ACM2	0.36/**0.55**/0.09	0.22/0.22/0	0.16/0.17/0	0.12/0.06/0
BouLac	0.34/0.41/0.10	0.20/0.14/0.01	0.15/0.02/0	0.09/0.01/0
MRF	0.37/0.41/**0.14**	**0.23/0.23/0.02**	**0.19/0.16**/0	**0.16/0.07**/0
MYNN2	0.38/0.40/0.02	0.21/0.08/0	0.16/0.001/0	0.12/0/0
YSU	**0.38**/0.40/0.09	0.21/0.15/0.003	0.16/0.06/0	0.12/0.02/0
FAR				
ACM2	0.39/0.28/0.80	0.64/0.43/1.00	0.76/0.54/1.00	0.85/0.84/1.00
BouLac	0.44/0.39/0.83	0.67/0.66/0.93	0.78/0.93/1.00	0.88/0.97/1.00
MRF	**0.38/0.24/0.74**	**0.62/0.34/0.88**	**0.72/0.46**/1.00	**0.78/0.77**/1.00
MYNN2	0.40/0.33/0.96	0.65/0.73/1.00	0.76/0.97/1.00	0.84/1.00/1.00
YSU	0.41/0.34/0.84	0.66/0.61/0.98	0.76/0.83/1.00	0.83/0.96/1.00
HSS				
ACM2	0.34/**0.60**/0.11	0.28/0.31/− 0.004	0.24/**0.26**/0	0.20/0.09/0
BouLac	0.31/0.47/0.11	0.25/0.17/0.01	0.22/0.01/− 0.002	0.15/− 0.001/0
MRF	0.36/0.49/**0.18**	**0.30/0.33/0.02**	**0.28**/0.25/− 0.002	**0.26/0.11**/− 0.001
MYNN2	**0.37**/0.47/− 0.03	0.27/0.09/− 0.02	0.23/− 0.02/− 0.01	0.19/− 0.01/− 0.003
YSU	0.36/0.47/0.09	0.27/0.19/− 0.01	0.24/0.07/− 0.004	0.20/0.01/− 0.002
PC				
ACM2	0.73/**0.86**/0.88	0.86/0.88/**0.94**	0.92/0.93/**0.98**	0.96/0.96/0.99
BouLac	0.71/0.82/0.86	0.85/0.86/0.94	0.92/0.91/0.97	0.96/0.96/0.99
MRF	**0.74**/0.85/**0.89**	**0.87/0.89**/0.94	**0.93/0.94**/0.97	**0.97/0.97/0.99**
MYNN2	0.73/0.83/0.85	0.86/0.86/0.93	0.92/0.91/0.97	0.96/0.95/0.97
YSU	0.73/0.83/0.87	0.85/0.86/0.94	0.92/0.92/0.97	0.96/0.95/0.99
POD				
ACM2	0.46/**0.65**/0.15	**0.37/0.26**/0	0.34/**0.21**/0	0.42/0.08/0
BouLac	0.47/0.56/0.20	0.34/0.19/0.01	0.30/0.03/0	0.26/0.01/0
MRF	0.47/0.47/**0.23**	0.36/0.26/**0.03**	**0.36**/0.18/0	**0.43/0.09**/0
MYNN2	0.51/0.49/0.04	0.36/0.11/0	0.31/0.01/0	0.29/0/0
YSU	**0.52**/0.50/0.16	0.37/0.19/0.005	0.32/0.08/0	0.30/0.03/0

Here the best/least skill experiments are highlighted/underlined

Table 4 shows the statistics of WS_{10m} for JUL14, AUG14, and JUL15. Simulations show IOA on the lower side of the acceptable range (IOA > 0.6 m s$-^{-1}$) most of the times. Bias lies on the upper side of the acceptable range (bias < 0.5 K). FB is on the lower side of the acceptable range (FB < 0.5). Like T_{2m}, experiments overestimate the forecast of WS_{10m} also (negative FB). In terms of statistics, MRF shows the best and BouLac the weakest performance of WS_{10m} among the experiments. ACM2 emerges as the second-best scheme, except for JUL15.

Figure 7c, d shows the temporal variation of domain-averaged LHF and sensible heat flux (SHF). These fluxes show an increasing trend with higher values during daytime having a peak during 0600 UTC–0900 UTC and the minimum during the night time, i.e., 1500 UTC–0000 UTC (Fig. 7c, d). Fluxes are very low during the nighttime; LHF is positive but less than 30 W m^{-2} and SHF is negative about − 10 W m^{-2}. Negative SHF during night time indicates that the model produces a warmer lower layer than the surface, which is well expected. The magnitude of flux is highest in MYNN2 and coherent with BouLac and YSU. BouLac, MYNN2, and YSU show the almost similar trend for LHF and SHF with a maximum up to 250 W m^{-2} and 170 W m^{-2}, respectively. MRF simulates the minimum fluxes than others; LHF and SHF less than 200 and 115 W m^{-2}, respectively. Fluxes for ACM2 are slightly higher but closer to MRF. Comparison of experiments with ERA5 shows that MRF and ACM2 are able to reproduce LHF during 1200 UTC 4 August–0300 UTC 6 August, and underestimate afterward. LHF values for ERA5 are maximum during 0300–0900 UTC 7 August (Fig. 7c). Experiments overestimate SHF throughout the simulation; however, MRF is closer to ERA5 than others (Fig. 7d). Overall, inter-comparison among the experiments indicates more than 60 W m^{-2} difference between

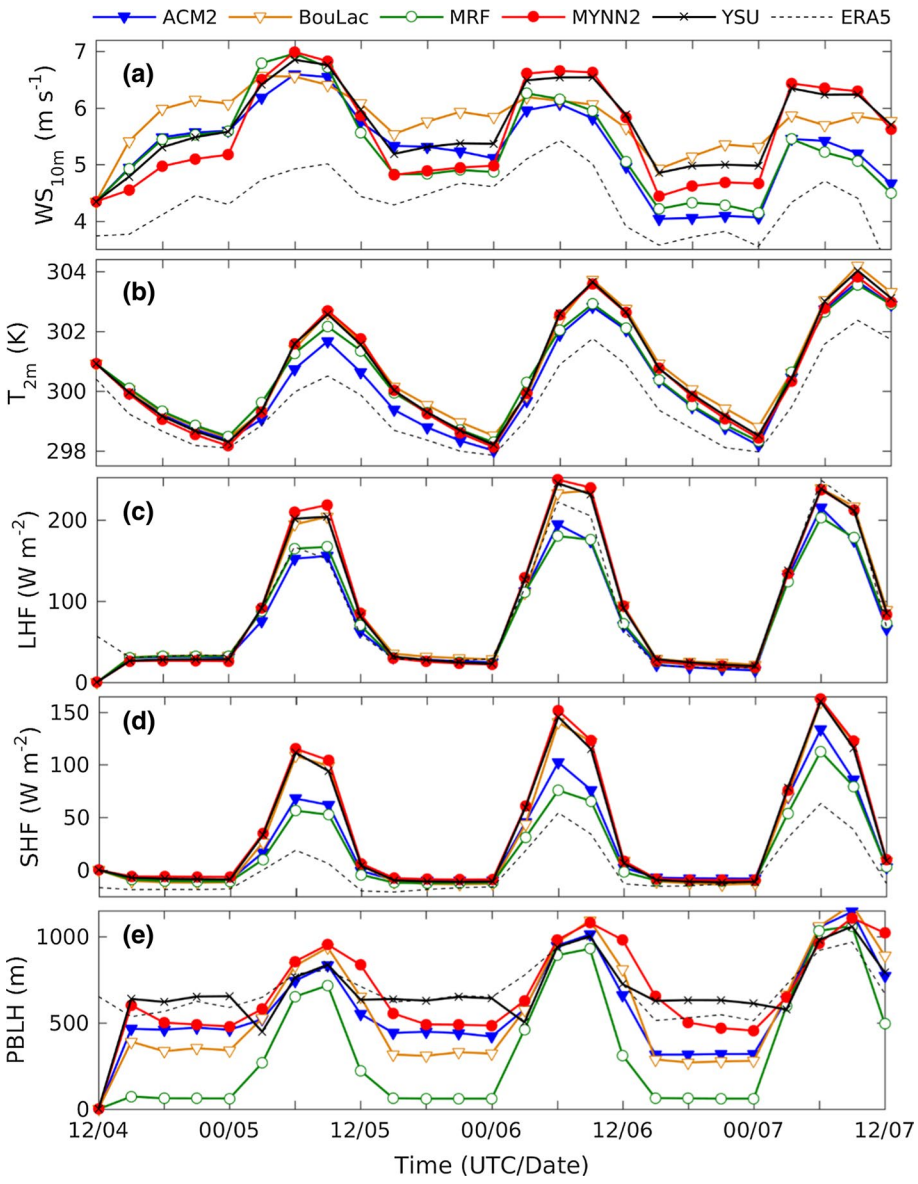

Fig. 7 Time series of domain averaged **a** wind speed 10 m above the surface (WS_{10m}), **b** temperature 2 m above the surface (T_{2m}), **c** latent heat flux (LHF), **d** sensible heat flux (SHF), and **e** planetary boundary layer height (PBLH). WS_{10m} and T_{2m} are compared with ERA5 data

the maximum flux values. Like experiments, ERA5 shows an increase in the total surface fluxes with time (Fig. 7c, d). The increase in total surface heat fluxes (SHF and LHF) increases the PBLH (Patil et al. 2013).

Figure 7e shows the temporal variation of domain-averaged PBLH. PBLH shows a consistent increase from 700 to 1106 m during the daytime as the rain rate decreases (Fig. 2). The differences between the peak PBLH values are varying between 100 and 250 m. PBLH for local schemes (MYNN2 and BouLac), nonlocal schemes (YSU and ACM2), and ERA5 are very similar during 0300 UTC to 0900 UTC, i.e., before afternoon, followed by a strong variation afterward (Fig. 7e). MRF simulates the lowest PBLH (< 1000 m) throughout the simulation (Fig. 7e). PBLH is the deepest for MYNN2 (900–1100 m) during the daytime, whereas, for YSU (550–650 m) during the nighttime (Fig. 7e). PBLH differences for MRF with others are higher (> 300 m) during nighttime than daytime (< 150 m) represents lower vertical mixing for MRF throughout the simulation. Higher vertical mixing transports more moisture and heat from the surface to the free atmosphere, and hence modulates the precipitation associated with the system (Wisse and Arellano 2004). These findings suggest that deep/shallow PBLH associated with strong/weak surface fluxes for local/nonlocal schemes favors more/less moisture transport, which in turn, may modulate the rainfall distribution.

During daytime, the development of the boundary layer is a result of heat transmission from the surface to the atmosphere and is strongly correlated to the surface SHF (Dang et al. 2016; Sathyanadh et al. 2017b). The nature of SHF magnitude attributes to lower PBLH for MRF and higher PBLH for BouLac and MYNN2 than others. However, same

Table 3 Statistical performance indices for 2 m temperature (T_{2m}) for JUL14, AUG14, and JUL15 with respect to ERA5

	ACM2	BouLac	MRF	MYNN2	YSU
AUG14					
IOA (>0.7)	**0.764**	0.716	0.738	0.715	0.723
Bias (<±0.5)	**0.724**	1.203	0.954	1.038	1.096
FB (<±0.5)	**−0.0024**	−0.0040	−0.0032	−0.0035	−0.0036
RMSE (<2)	**1.625**	1.921	1.760	1.896	1.884
JUL14					
IOA (>0.7)	**0.613**	0.590	0.569	0.590	0.587
Bias (<±0.5)	**1.398**	1.517	1.824	1.482	1.522
FB (<±0.5)	**−0.0046**	−0.0050	−0.0061	−0.0049	−0.0050
RMSE (<2)	**1.985**	2.121	2.295	2.134	2.143
JUL15					
IOA (>0.7)	**0.547**	0.535	0.530	0.532	0.534
Bias (<±0.5)	**1.177**	1.241	1.372	1.241	1.344
FB (<±0.5)	**−0.0039**	−0.0041	−0.0045	−0.0041	−0.0045
RMSE (<2)	**1.901**	1.980	2.070	2.090	2.101

The numbers in bracket in column 1 shows the acceptable values for the respective statistics. Here the best/least skill experiments are highlighted/underlined

Table 4 Statistical performance indices for 10 m wind speed (WS_{10m}) for JUL14, AUG14, and JUL15 with respect to ERA5

	ACM2	BouLac	MRF	MYNN2	YSU
AUG14					
IOA (>0.6)	0.620	0.566	**0.622**	0.574	0.579
Bias (<±0.5)	**0.946**	1.459	0.950	1.228	1.376
FB (<±0.5)	− 0.1974	− 0.2879	**− 0.1933**	− 0.2874	− 0.2730
RMSE (<2)	**1.853**	2.181	1.870	2.128	2.153
JUL14					
IOA (>0.6)	0.592	0.533	**0.604**	0.552	0.555
Bias (<±0.5)	0.912	1.243	**0.685**	1.029	1.147
FB (<±0.5)	− 0.1412	− 0.1895	**− 0.1170**	− 0.1687	− 0.1803
RMSE (<2)	2.117	2.382	**2.001**	2.254	2.298
JUL15					
IOA (>0.6)	0.503	0.4424	**0.536**	0.521	0.481
Bias (<±0.5)	1.149	1.412	**0.831**	0.882	1.121
FB (<±0.5)	− 0.1759	− 0.2135	**− 0.1386**	− 0.1484	− 0.1767
RMSE (<2)	2.157	2.368	**1.998**	2.029	2.191

The numbers in bracket in column 1 shows the acceptable values for the respective statistics. Here the best/least skill experiments are highlighted/underlined

reason is not applicable for YSU, with SHF values in the same range as for BouLac and MYNN2 (95–160 W m^{-2}) and is reasonably higher (~ 50 W m^{-2}) than ACM2. This variation in PBLH for YSU can be attributed to the explicit treatment entrainment process at the top of the boundary layer (Sect. 3). YSU shows a relatively moist air above 900 hPa than BouLac and MYNN2 (Fig. 9). Moist air entrainment reduces the PBLH (Sathyanadh et al. 2017b) and is responsible for shallower PBLH for YSU than BouLac and MYNN2 during the daytime (Fig. 7e). During night time, when SHF is mostly negative, PBLH must be dependent on the variation in the wind shear within the lower layers.

4.4 Vertical structures

Figure 8 compares the vertical profiles of the simulated wind speed, temperature, and specific humidity with radiosonde data obtained from University of Wyoming (WUR) at a fixed location Patna (25.60°N; 85.10°E). Here, WRF values are extracted at the point nearest to 25.60°N; 85.10°E. WUR data sets are available only at 0000 UTC and Patna location does not fall within the core region of the MD, but, however, exists within the simulation domain and is closer to the system particularly at 0000 UTC 5 August. The comparison of simulated wind speed with WUR shows that the model underestimates it within 900–600 hPa at 0000 UTC 5 August (Fig. 8a) and above 400 hPa at 0000 UTC 7 August (Fig. 8c). The simulated air temperature below 900 hPa is relatively warmer than WUR at 0000 UTC 7 August (Fig. 8f) and closer to MRF at 0000 UTC 5 August (Fig. 8d). Further simulated lower layers (below 900 hPa) are relatively drier than WUR (Fig. 8g–i). Although, the model does not match the WUR data exactly, it is able to capture the vertical profiles.

Discussions in Sects. 4.2–4.3 have shown that MRF has better skill than others up to day 3. Therefore, to further compare the vertical structure of the other experiments, MRF is used as a benchmark. Figure 9 shows the temporal variation of the differences of the domain-averaged wind speed between experiments and MRF. Experiments show a relatively lower variation in the wind speed (about −0.5 to 0.5 m s^{-1}) above 800 hPa during the initial 18 h, i.e., 1200 UTC 4 August–0600 UTC 5 August. Except for ACM2, the variations in the mid-tropospheric (800–500 hPa) wind differences are relatively weak (between -0.5 and 0.5 m s^{-1}) during 0600 UTC 5 August–0600 UTC 6 August and strong (> 1 m s^{-1}) afterward. Higher wind speed after 0600 UTC 6 August shows the increase of wind shear in the mid-troposphere. The upper tropospheric (above 300 hPa) wind speeds for BouLac, MYNN2, and YSU are much stronger (> 2 m s^{-1}) than MRF. ACM2 simulates a slightly weaker wind (~ 1 m s^{-1}) between 800 and 600 hPa, and about 0.5–2 m s^{-1} stronger wind above 600 hPa compared to MRF. The variations in the wind speed directly affect the availability of moisture. The presence of moisture may also vary due to phase change particularly in the middle troposphere which modulates the temperature.

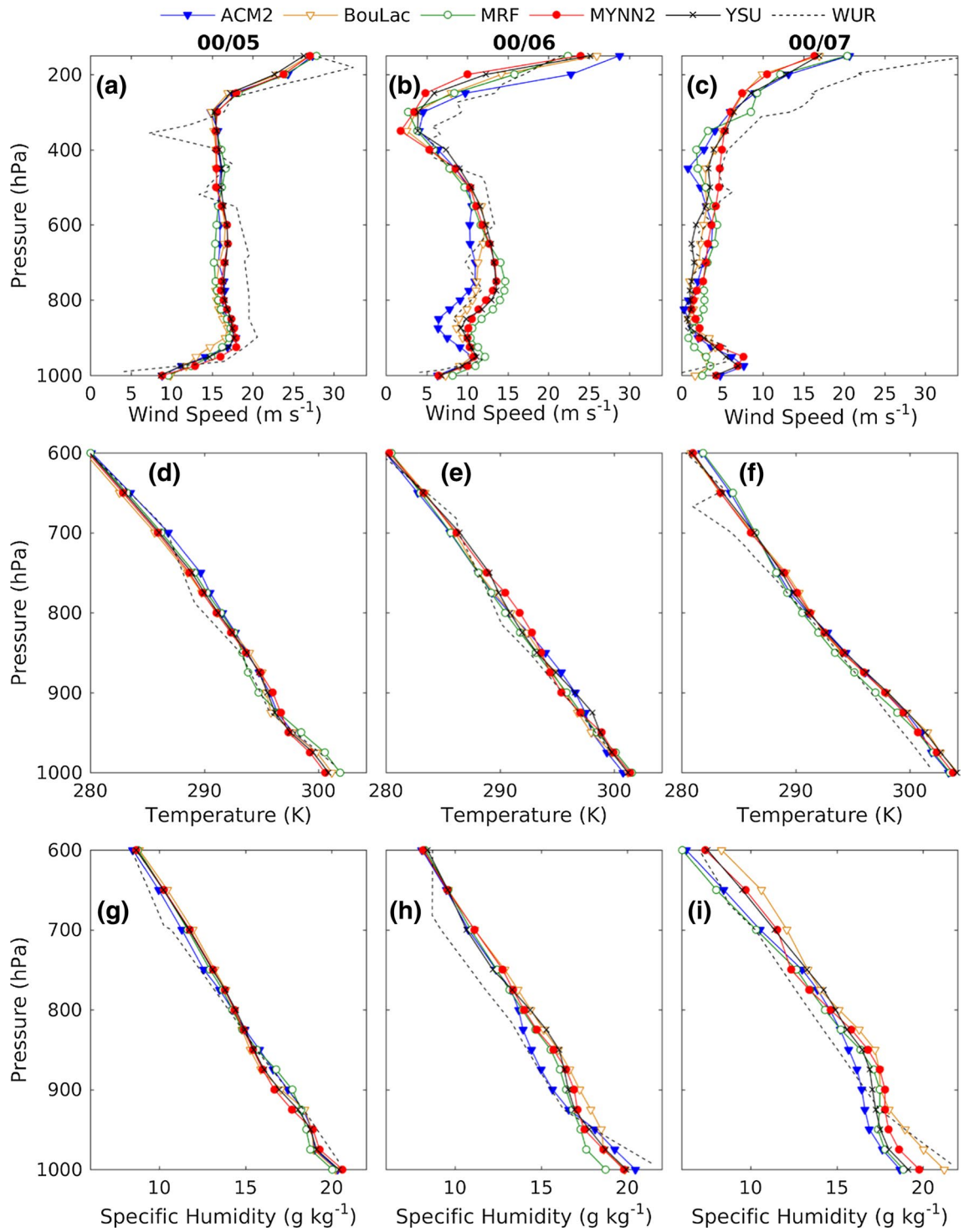

Fig. 8 Validation of the vertical profiles of the simulated **a–c** wind speed, **d–f** temperature, and **g–i** specific humidity with radiosonde data from University of Wyoming (WUR) at Patna (25.60°N; 85.10°E). Here the first, second and third column shows the profile at 0000 UTC 5 August 2014, 0000 UTC 6 August 2014, and 0000 UTC 7 August 2014, respectively

Experiments show almost similar pattern within the lower layers; a very thin layer (~925 hPa) of weaker wind underlying a stronger wind layer up to 800 hPa than MRF, except BouLac. BouLac shows a thin layer of stronger wind underlying a weaker winds layer than MRF (Fig. 9b). The thin layer of positive wind between 1000 and 800 hPa is weaker for ACM2 and BouLac (~0.5 m s^{-1}) than others, which reduces the wind shear. The presence of relatively

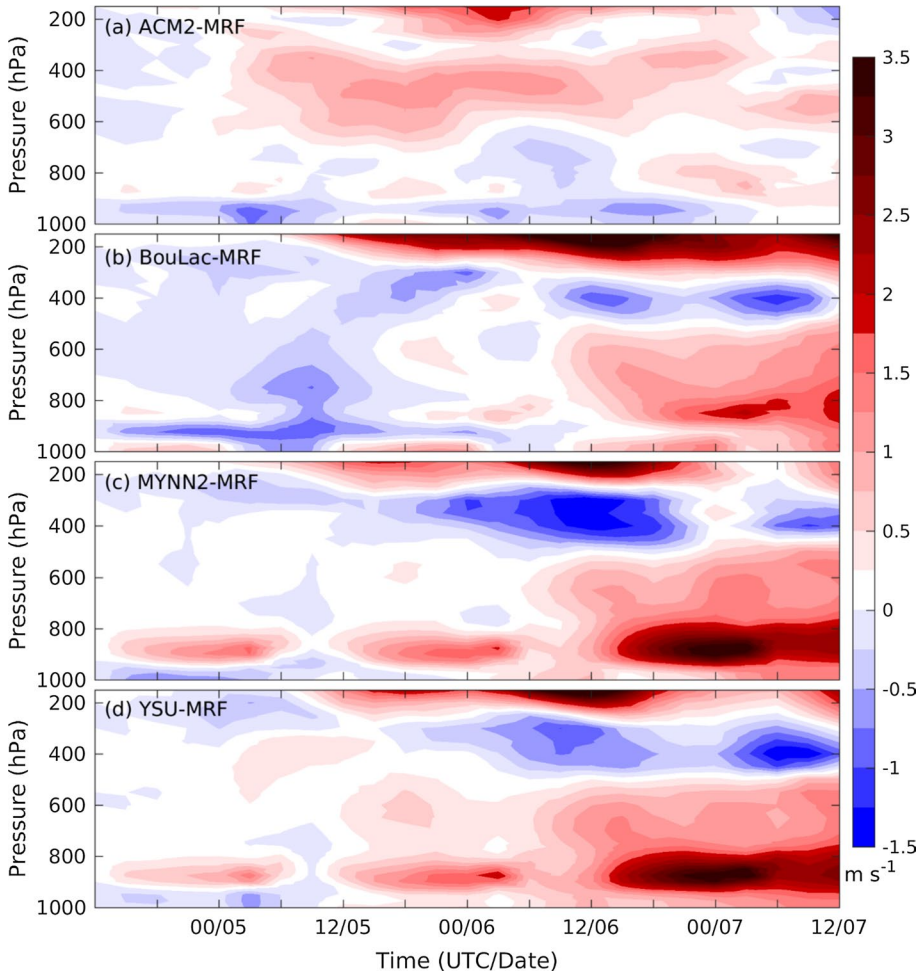

Fig. 9 Time-series of vertical distribution of domain-averaged differences in the wind speed for **a** ACM2-MRF, **b** BouLac-MRF, **c** MYNN2-MRF, and **d** YSU-MRF

stronger wind near the surface (Fig. 7a) and lower model levels (Fig. 9b) for BouLac and weaker wind above reduces the wind shear and causes a shallower PBLH for BouLac than ACM2 during night time. Similarly, a stronger wind shear associated with YSU deepens the PBLH than others (Fig. 7e).

Figure 10 shows the time–pressure distribution of the difference of specific humidity (shaded) and temperature (contours) from MRF. Here, positive and negative temperature values are represented with solid and dashed lines, respectively. Experiments show that, except for ACM2, increase (decrease) in temperature within 850–300 hPa is associated with the decrease (increase) in specific humidity. For ACM2, variations in specific humidity above 850 hPa are much coherent with wind speed; increase/decrease in wind speed (Fig. 9a) is associated with the decrease/increase in specific humidity (Fig. 10a). Above 300 hPa, specific humidity does not vary much (<0.1 g kg^{-1}); however, the temperature is mostly higher than MRF, except ACM2 (Fig. 10). For ACM2, the temperature is cooler above 600 hPa than MRF (Fig. 10a). Further, except ACM2, other experiments show a warmer air temperature within the lower layers (1000–850 hPa) during the daytime, i.e., 0300–1500 UTC (Fig. 10). In addition, MRF produces drier lower layers (1000–850 hPa) than others (Fig. 10; Figs. S6, S7). To further investigate this warming within the lower layer, Fig. 11 shows the longitude–pressure plots for the difference of temporally and latitudinally averaged air temperature between the experiments and MRF. The time averaging is obtained during 0300–1500 UTC 5 August. During this period, most of the rainfall occurred over 22°N–25°N, and 80°E–84°E; therefore, latitudinal average is obtained for 22°N–25°N. It is found that ACM2 and MRF show the strongest and weakest rain, respectively (Fig. 2) with the coolest lower layers for ACM2 (Figs. 7b, 10) than others. BouLac, MYNN2, and YSU show cooler lower layers over 80°E–84°E and warmer layers to the west of 80°E than MRF. Therefore, the presence of stronger rainfall associated with cold pool leading to cooler temperatures at the surface over the region, however, warmer air temperature to the west of intense convection, is responsible for overall warmer lower layers for BouLac, MYNN2 and YSU than MRF (Figs. 7b, 10).

It is well known that MDs are associated with convergence within the boundary layer and divergence above. The

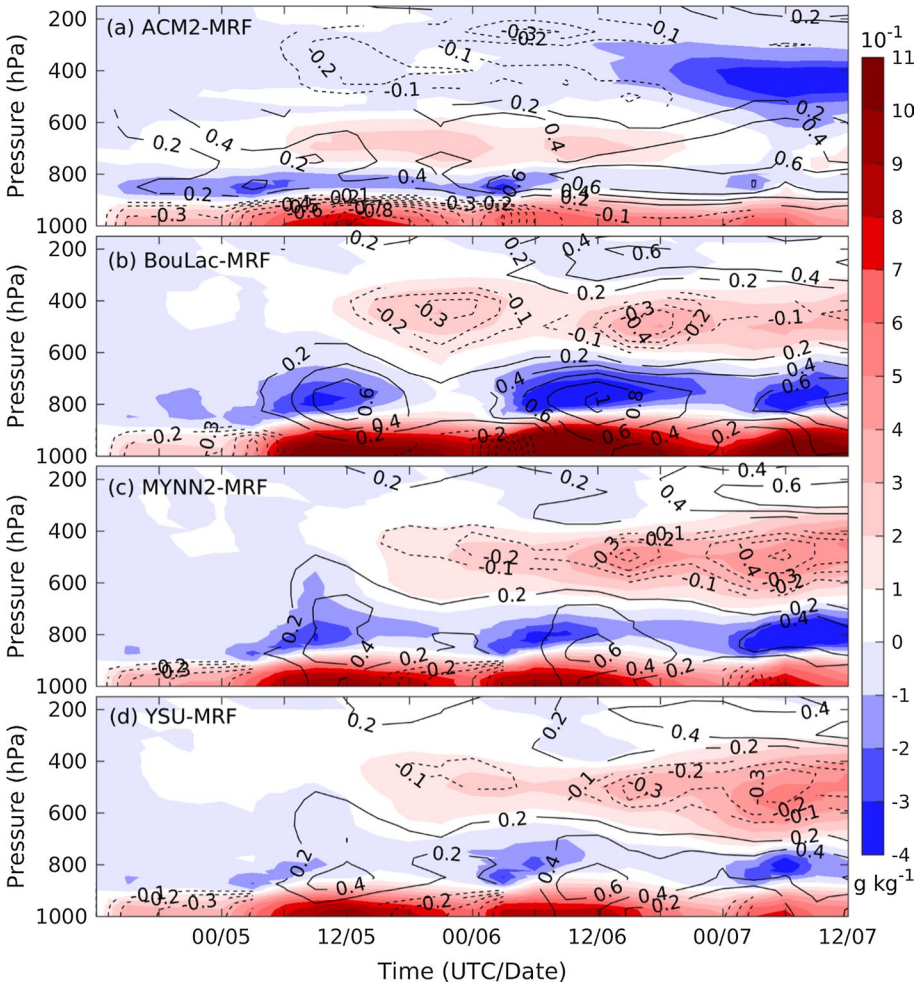

Fig. 10 Time-series of vertical distribution of domain-averaged differences in the specific humidity (shaded; g kg^{-1}) and temperature (contours; K) for **a** ACM2-MRF, **b** BouLac-MRF, **c** MYNN2-MRF, and **d** YSU-MRF. Here positive and negative temperature differences are represented with solid and dashed line contours

presence of stronger wind within lower levels (< 850 hPa) presents more convergence for experiments, particularly for MYNN2 and ACM2, compared to MRF. Moisture distribution within the boundary layer, i.e., surface–850 hPa, is affected by convergence, and hence the amount of moisture transport towards the MD center. Figure 12 illustrates the vertically integrated moisture transport within the layers below 850 hPa. Here, vertically integrated moisture transport is defined as (Ma et al. 2018)

$$\mathrm{MT} = \sqrt{\left(\frac{1}{g}\int_{P_s}^{850} qu\mathrm{d}p\right)^2 + \left(\frac{1}{g}\int_{P_s}^{850} qv\mathrm{d}p\right)^2}.$$

Here, u and v are the zonal and meridional components of the wind speed (m s^{-1}), q is specific humidity (kg kg^{-1}), and P_s is the surface pressure (hPa).

It is found that the lowest moisture transport for MRF (Fig. 12) causes relatively dry boundary layer for MRF than others (Fig. 10). YSU simulates the highest moisture transport within the boundary layer with a maximum above 185 kg m^{-1} s^{-1} during 1800 UTC to 2100 UTC 6 August (Fig. 12). However, the lower vertical mixing for YSU during the daytime (Fig. 7e) reduces the vertical transport of moisture from the surface to upper layers, and hence reduces the overall precipitation (Fig. 2). The magnitude of moisture fluxes for MYNN2 and BouLac is close to YSU. Moisture transport for ACM2 is much closer to MRF. From 1200 UTC 6 August onwards, the moisture transport from YSU, BouLac, and MYNN2 is about 60 kg m^{-1} s^{-1} stronger than MRF and ACM2 (Fig. 12); however, the amount of rain rate does not show any significant variation (Fig. 2) for these experiments.

Moisture transport shows an increasing trend during night time (1200–0000 UTC) and a decreasing trend during daytime (0000–0600 UTC). Here, the first peak of moisture transport during 0600 UTC 5 August–0600 UTC 6 August matches well with the rain rate. During 0600 UTC 5 August–0000 UTC 6 August, when moisture transport shows an increase from 81 to 148 kg m^{-1} s^{-1} (Fig. 12), a continuous rain with a rate above 17 mm day^{-1} occurred for YSU (Fig. 2). During 0000 UTC 6 August–0600 UTC 6 August,

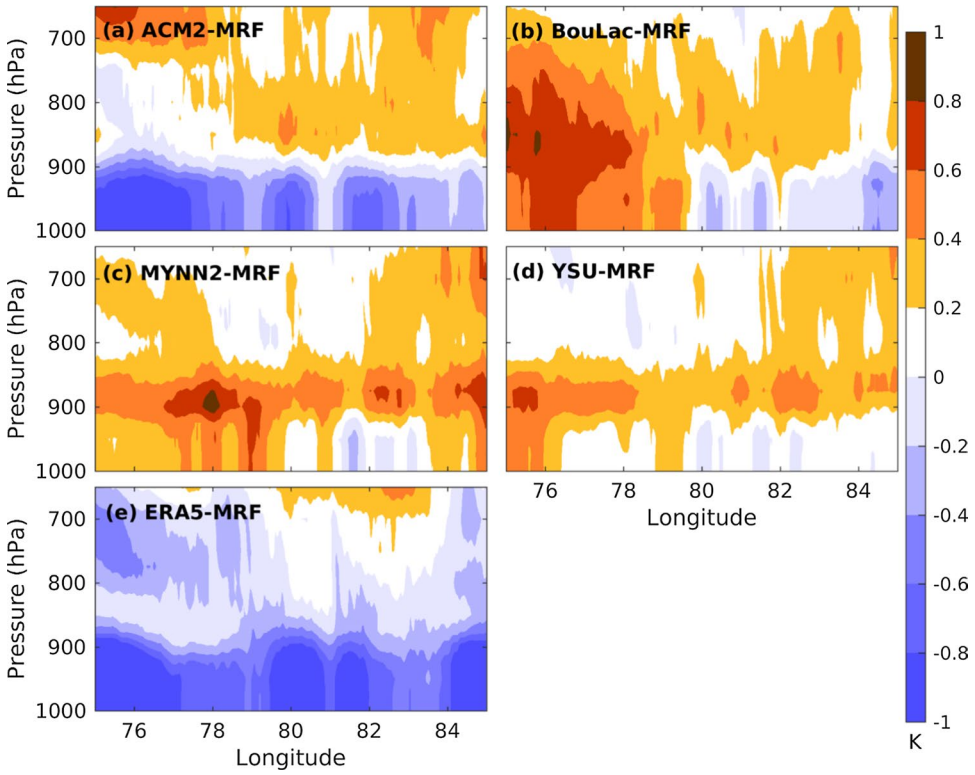

Fig. 11 Difference of temporally and latitudinally averaged air temperature (K) for **a** ACM2, **b** BouLac, **c** MYNN2, **d** YSU, and **e** ERA5 from MRF. Temporal average: 0300 UTC 5 August–1500 UTC 5 August; latitudinal average: 22–25°N

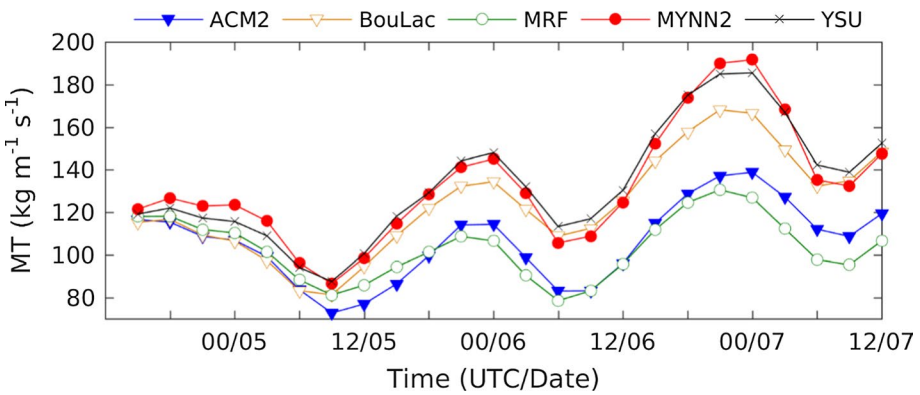

Fig. 12 Time series of domain-averaged vertically integrated moisture transport within the lower layer (surface—850 hPa)

as the moisture transport decreased to 108 kg m^{-1} s^{-1} (Fig. 12), rain rate decreased to 9 mm day^{-1} with the highest rain rate for BouLac (Fig. 2). From 0600 UTC 6 August onwards, moisture transport increase up to 168 kg m^{-1} s^{-1} at 2100 UTC 6 August, and further decreased to 148 kg m^{-1} s^{-1} at 1200 UTC 7 August (Fig. 12); however, rain rate shows a decrease from 9 to 2 mm day^{-1} during this period (Fig. 2). The increase in the moisture transport is facilitated by strong specific humidity (Fig. 10) and wind speed (Fig. 9) associated with boundary layer extent from 1200 UTC 6 August onwards. However, the presence of strong wind shear within the mid-troposphere (Figs. 9, 13b) weakens the convective structure of the system and reduces the rainfall.

It has been discussed earlier that model shows a distinct variation in wind speed before and after 1200 UTC 6 August for AUG14 case (Fig. 9). The inter-comparison of experiments shows a relatively lower variation in the mid-tropospheric wind speed (− 0.5 to 0.5 m s^{-1}) during 0600 UTC 5–6 August than variations afterward > 1 m s^{-1} (Fig. 9). These variations in the wind speed indicated that the mid-tropospheric wind shear is relatively weaker during 5–6 August than 6–7 August. Figure 13 compares the domain- and time-averaged simulated wind speed, equivalent potential temperature (Θ_e), and relative humidity with ERA5 data. The time averaging is obtained during 0000 UTC 5 August–0000 UTC 6 August (Fig. 13a, c, e) and 1200 UTC 6 August–1200 UTC 7 August (Fig. 13b, d, f). Simulated wind speeds show a similar trend as shown by ERA5 with a relatively weaker wind shear during 0000 UTC 5 August–0000 UTC 6 August than 1200 UTC 6 August–1200

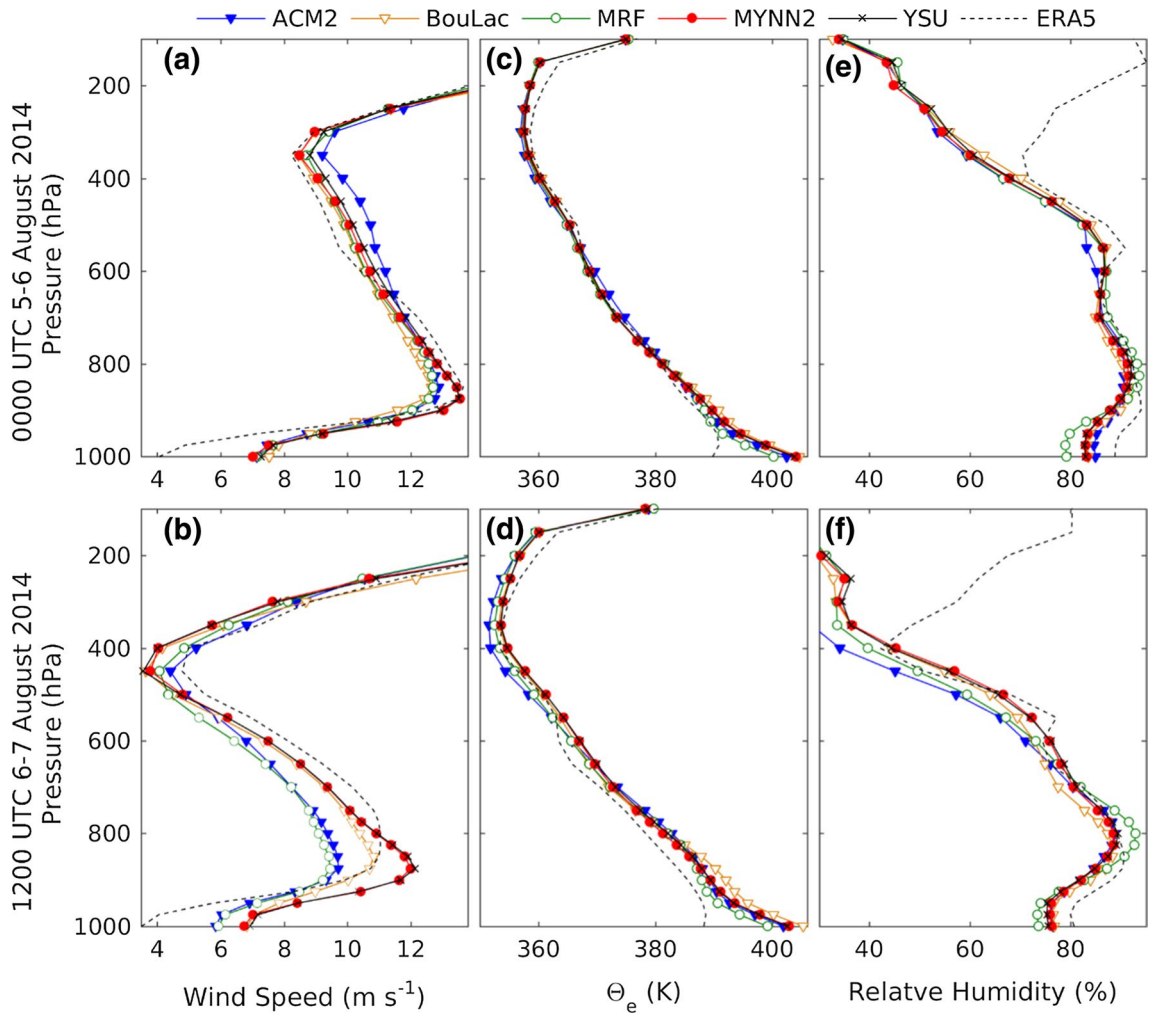

Fig. 13 Validation of the vertical profiles of the simulated **a**, **b** wind speed, **c**, **d** equivalent potential temperature (Θ_e), and **e**, **f** relative humidity with ERA5 data. Profiles are temporally and spatially averaged. First and second rows are temporally averaged during 0000 UTC 5–6 August 2014 and 1200 UTC 6–7 August 2014, respectively

UTC 7 August. During 0000 UTC 5 August–0000 UTC 6 August (1200 UTC 6 August–1200 UTC 7 August), wind speed decreased from 13 to 8 m s^{-1} (11–4 m s^{-1}) between 850 and 400 hPa (Fig. 13a, b). The magnitude of wind shear does not vary much among the experiments during 0000 UTC 5 August–0000 UTC 6 August (Fig. 13a). However, during 1200 UTC 6 August–1200 UTC 7 August, wind shear is the strongest for YSU and the weakest for MRF (Fig. 13b). In addition, wind shear for MYNN2 and ACM2 is very similar to that for YSU and MRF, respectively (Fig. 13b). The model simulates a relatively warmer Θ_e than ERA5 particularly within the lower layers (Fig. 13c, d). Further, the model simulates relative lower humidity within 1000–800 hPa and 400–150 hPa than ERA5 (Fig. 13e, f). Overall, variables show a good coherence with ERA5 except for variations within 1000–900 hPa. Notable differences between the model and ERA5 are found for relative humidity above 400 hPa (Fig. 13e, f).

5 Summary

The WRF–ARW model is used to assess the sensitivity of MD characteristics to the PBL parameterizations. A total of 5 PBL schemes, three nonlocal K profile-based schemes (ACM2, MRF, and YSU) and two local TKE-based schemes (BouLac and MYNN2), are investigated in this study. The sensitivity experiments are repeated for three MDs, i.e., JUL14 (0000 UTC 21 July–0000 UTC 24 July 2014), AUG14 (1200 UTC 4 August–1200 UTC 7 August 2014), and JUL15 (0000 UTC 27 July–0000 UTC 30 July 2015). The selected MDs belong to different parts of the country. JUL15 was developed over the northwest part of India which

moved northward during its intensification. JUL14 and AUG14 were developed over the northeast part of the country and progressed westward and northwest, respectively during the simulation period. Further, systems differ in terms of progress over land. Although, the two outer domains are almost similar, due to computational limits, the inner-most domain varies from one system to other. A series of five simulations with each MD are carried out to examine the sensitivity of simulated MDs to the PBL parameterizations at 3-km horizontal resolution. All the three above-mentioned cases are analyzed to conclude the results. However, only AUG14 is discussed comprehensively with the plots for other MDs provided in supporting information.

This study mainly focuses on the sensitivity of rainfall, surface, and vertical parameters associated with MDs to the PBL parameterizations. The model simulations underestimate the rain rate compared with GPM data. The comparison among the experiments shows that the highest and lowest rain rates are associated with BouLac and MRF, respectively. Statistical analysis of the simulated rainfall with GPM suggests MRF and ACM2 as the two best schemes among all the experiments. Rainfall forecast skill is consistently poor for local schemes, i.e., MYNN2 and BouLac than others.

Comparison of surface variables (WS_{10m} and T_{2m}) with ERA5 shows that the model overestimates these variables; however, MRF and ACM2 have better forecast skill of WS_{10m} and T_{2m}, respectively. BouLac simulates the maximum WS_{10m} during the night and overestimate > 1 m s^{-1} compared to ERA5. Further, the variations of PBLH show a distinct pattern during day and night time. During the daytime, mixing is highest for local schemes, minimum for MRF, and almost similar for ACM2 and YSU. During the nighttime, the change in wind shear explains the more decrease in PBLH for BouLac than YSU.

Vertical distribution of wind speed shows that wind shear is relatively lower (higher) for BouLac (YSU) than others. Lower (higher) wind shear reduces (enhances) the mixing and hence decreases (increases) the PBLH for BouLac (YSU) during night time. For all these experiments, the increase (decrease) in the temperature in the mid-troposphere is associated with heating (cooling) due to decrease (increase) of moisture due to phase change except for ACM2. Role of wind distribution dominates in the spread of moisture over the study region for ACM2. Results indicate relatively drier and warmer boundary layer for MRF due to less convergence (reducing the incursion of moisture), resulting in a shallower PBLH than others. Shallower PBLH limits the mixing within a thin layer and leads to a warmer boundary layer for MRF than others.

A moist boundary layer associated with a strong wind leads to more moisture transport, but more moisture transport does not always favor rainfall. Results suggest that moist boundary layer associated with strong divergence in the upper atmosphere is favorable for the rain associated with MDs, and the presence of strong wind shear within the mid-troposphere reduces the convective activity, hence reducing the rain amount. Therefore, the moist boundary layer associated with stronger divergence in the upper layers and weak wind shear in the mid-troposphere favors the convective activity, and hence produces stronger systems with intense rainfall.

Results, particular reference to rainfall over the Indian region, suggest strong confidence in the model forecast based on nonlocal MRF PBL scheme. Further, local schemes such as Boulac and MYNN2 produce the least skill scores with relatively smaller differences between them. Finally, to obtain more accurate rainfall forecast skill of the model, it is advisable to increase the horizontal resolution of the model further finer (~ 1 km) to resolve PBL, convection and topographical features of the Indian region.

Acknowledgements The authors want to express their gratitude to the Indian Meteorological Department (IMD) and National Aeronautics and Space Administration (NASA)-Precipitation Measurement Mission (GPM) for providing the daily rainfall data, National Centers for Environmental Prediction (NCEP)–National Oceanic and Atmospheric Administration (NOAA) for initial and boundary condition, European Center for Medium-Range Weather Forecasts (ECMWF) for providing high resolution reanalysis data (i.e., ERA5) for validation (Contains modified Copernicus Climate Change Service Information), and National Centre for Atmospheric Research (NCAR) for using their WRF–ARW model for carrying out this study. We are thankful for the support of Indian Institute of Technology Bhubaneswar, Department of Science and Technology (DST), Government of India (RP-132) and Ministry of Earth Sciences (MoES), Government of India (RP088) for carrying out this research work. Figures are created with MATLAB (Version 2015a).

Appendix 1: Methods for dichotomous forecasts

	Observed		
		Yes	No
Forecast	Yes	*a*	*b*
	No	*c*	*d*

Here, '*a*' represents the event forecast to occur and did occur, i.e., hits, '*b*' represent the event forecast to occur but did not occur, i.e., false alarms, '*c*' represent the event forecast no to occur but did occur, i.e., misses, '*d*' represent the event forecast no to occur and did not occur, i.e., correct no forecast

The standard verification methods used for rainfall validation are discussed as below

Equitable Threat Score (ETS)

Equitable Threat Score (ETS) is defined as the fraction of correctly predicted observed and/or forecast events after removing the contribution from hits by chance (a_{ref}) and is defined by

$$\text{Equitable Threat Score (ETS)} = \frac{a - a_{\text{ref}}}{a - a_{\text{ref}} + b + c}, \quad a_{\text{ref}} = \frac{(a+b)\times(a+c)}{a+b+c+d}. \tag{1}$$

ETS vary between $-1/3$ and 1, with perfect score equal to 1. ETS equal to zero represents no skill.

False alarm rate (FAR)

False alarm rate (FAR) is the ratio of the number of events actually did not occur (b) to the number of forecasted 'yes', i.e., $a+b$, and is defined as

$$\text{FAR} = \frac{b}{a+b}. \tag{2}$$

The smaller FAR indicates higher accuracy of forecast. FAR vary between 0 and 1 and zero indicates the perfect score.

Heidke Skill Score (HSS)

$$\text{HSS} = \frac{2(ad - bc)}{(a+c)(c+d) + (a+b)(b+d)}. \tag{3}$$

Percent correct (PC)

Percent correct (PC) is defined as the ratio of number of correct events ($a+d$) to the total number of events.

$$\text{PC} = \frac{a+d}{a+b+c+d} \tag{4}$$

It ranges between 0 and 1. Larger PC indicates the more accurate forecast. Hence, PC equal to 1 is the perfect score.

Probability of detection (POD)

Probability of detection (POD) indicates the fraction of observed 'yes' events forecasted correctly (a) to the number of observed 'yes' events ($a+c$) and is defined as

$$\text{POD} = \frac{a}{a+c} \tag{5}$$

POD ignores the event forecast to occur but did not occur actually, i.e., b and is sensitive to event forecast to occur and did occur actually, i.e., a. Larger POD values indicate the less number of events that were forecasted not to occur but did occur, i.e., c. It varies between 0 and 1 and POD equals to 1 is the perfect score.

Critical Success Index (CSI)

It is also known as threat score. It measures the fraction of observed and/or forecast events and indicated how well the forecasted 'yes', i.e., a, events, correspond to the observed 'yes', i.e., $a+b+c$, events and is defined as

$$\text{Critical Success Index (CSI)} = \frac{a}{a+b+c}. \tag{6}$$

It varies between 0 and 1, where 0 indicates no skill and 1 indicates the perfect score.

Appendix 2: Performance indicators for meteorological parameters

Index of agreement (IOA)

The index of agreement (IOA) measures the degree to which the model predictions are free from error and is expressed as (Willmott 1981)

$$\text{IOA} = 1 - \frac{\sum_{i=1}^{N}\left(O_i - P_i\right)^2}{\sum_{i=1}^{N}\left(\left|P_i - \overline{O}\right| + \left|O_i - \overline{O}\right|\right)^2}. \tag{7}$$

Here, O_i, P_i, $\overline{O}$, and $\overline{P}$ are observed data, predicted data, mean observed and mean predicted data, respectively. IOA has a theoretical range of 0 and 1, where 1 indicates the perfect match and 0 connotes the complete disagreement between observed and predicted values

Bias

Bias measures the sign of the errors of the predicted values and is defined as

$$\text{Bias} = \overline{P} - \overline{O}. \tag{8}$$

Positive (negative) value of bias implies overpredicted (underpredicted) model values.

Fractional bias (FB)

Fractional bias (FB) is the normalized bias and is defined as

$$\text{FB} = \frac{\overline{O} - \overline{P}}{0.5(\overline{O} + \overline{P})}. \tag{9}$$

FB varies between +2 and −2. Negative FB shows overestimation, whereas positive FB shows underestimation by model.

Root mean square error (RMSE)

Root mean square error (RMSE) measures the difference between the predicted and observed values and is defined as

$$\mathrm{RMSE} = \sqrt{\frac{\sum_{i=1}^{N}\left(P_i - O_i\right)^2}{N}}. \tag{10}$$

References

Avolio E, Federico S, Miglietta MM et al (2017) Sensitivity analysis of WRF model PBL schemes in simulating boundary-layer variables in southern Italy: an experimental campaign. Atmos Res 192:58–71

Basu S, Raman S, Mohanty UC, Rajagopal EN (1999) Influence of the planetary boundary layer physics on medium-range prediction of monsoon over India. Pure Appl Geophys 155:33–55

Basu S, Iyenger GR, Mitra AK (2002) Impact of a nonlocal closure scheme in a simulation of a monsoon system over India. Mon Weather Rev 130:161–170

Bougeault P, Lacarrere P (1989) Parameterization of orography-induced turbulence in a Mesobeta-Scale Model. Mon Weather Rev 117:1872–1890

Bryan GH, Morrison H (2012) Sensitivity of a simulated squall line to horizontal resolution and parameterization of microphysics. Mon Weather Rev 140:202–225

Cha D-H, Lee D-K, Hong S-Y (2008) Impact of boundary layer processes on seasonal simulation of the East Asian summer monsoon using a Regional Climate Model. Meteorol Atmos Phys 100:53–72

Cohen AE, Cavallo SM, Coniglio MC, Brooks HE (2015) A review of planetary boundary layer parameterization schemes and their sensitivity in simulating southeastern US cold season severe weather environments. Weather Forecast 30:591–612

Dang R, Li H, Liu Z, Yang Y (2016) Statistical analysis of relationship between daytime lidar-derived planetary boundary layer height and relevant atmospheric variables in the semiarid region in Northwest China. Adv Meteorol 2016:5375918

Deshpande NR, Kulkarni A, Kumar KK (2012) Characteristic features of hourly rainfall in India. Int J Climatol 32:1730–1744

Dimri AP, Chevuturi A, Niyogi D et al (2017) Cloudbursts in Indian Himalayas: a review. Earth Sci Rev 168:1–23

Efstathiou GA, Zoumakis NM, Melas D et al (2013) Sensitivity of WRF to boundary layer parameterizations in simulating a heavy rainfall event using different microphysical schemes. Effect on large-scale processes. Atmos Res 132–133:125–143

Emery C, Tai E, Yarwood G (2001) Enhanced meteorological modeling and performance evaluation for two Texax ozone episodes. Prepared for the Texas Natural Resource Conservation Commission. ENVIRON International Corporation, Novato

Flaounas E, Bastin S, Janicot S (2011) Regional climate modelling of the 2006 West African monsoon: sensitivity to convection and planetary boundary layer parameterisation using WRF. Clim Dyn 36:1083–1105

Fletcher JK, Parker DJ, Hunt KMR et al (2018) The interaction of Indian monsoon depressions with northwesterly midlevel dry intrusions. Mon Weather Rev 146:679–693

Goswami BN (1987) A mechanism for the west-north-west movement of monsoon depressions. Nature 326:376–378

Gunwani P, Mohan M (2017) Sensitivity of WRF model estimates to various PBL parameterizations in different climatic zones over India. Atmos Res 194:43–65

Hill KA, Lackmann GM (2009) Analysis of idealized tropical cyclone simulations using the weather research and forecasting model: sensitivity to turbulence parameterization and grid spacing. Mon Weather Rev 137:745–765

Holton JR (2004) An introduction to dynamic meteorology, 4th edn. Elsevier Academic Press, Amsterdam

Hong S-Y, Pan H-L (1996) Nonlocal boundary layer vertical diffusion in a medium-range forecast model. Mon Weather Rev 124:2322–2339

Hong S-Y, Noh Y, Dudhia J (2006) A new vertical diffusion package with an explicit treatment of entrainment processes. Mon Weather Rev 134:2318–2341

Hou AY, Kakar RK, Neeck S et al (2014) The global precipitation measurement mission. Bull Am Meteorol Soc 95:701–722

Hunt KMR, Turner AG (2017) The effect of horizontal resolution on Indian monsoon depressions in the Met Office NWP model. Q J R Meteorol Soc 143:1756–1771

Hunt KMR, Turner AG, Inness PM et al (2016) On the structure and dynamics of Indian monsoon depressions. Mon Weather Rev 144:3391–3416

IMD (2015) Monsoon 2014: a report. In: Pai DS, Bhan SC (eds) IMD Met. Monograph, ESSO Document No. ESSO/IMD/SYNOPTIC MET/01(2015)/17, National Climate Centre; India Meteorological Department, New Delhi

Krishnamurthy V, Ajayamohan RS (2010) Composite structure of monsoon low pressure systems and its relation to Indian rainfall. J Clim 23:4285–4305

Krishnamurti TN, Pattnaik S, Bhaskar Rao DV (2007) Mesoscale moisture initialization for monsoon and hurricane forecasts. Mon Weather Rev 135:2716–2736

Ma Y, Lu M, Chen H et al (2018) Atmospheric moisture transport versus precipitation across the Tibetan Plateau: a mini-review and current challenges. Atmos Res 209:50–58

Nakanishi M, Niino H (2004) An improved Mellor-Yamada level-3 model with condensation physics: its design and verification. Bound Layer Meteorol 112:1–31

Nakanishi M, Niino H (2009) Development of an improved turbulence closure model for the atmospheric boundary layer. J Meteorol Soc Jpn 87:895–912

Patil MN, Patil SD, Waghmare RT, Dharmaraj T (2013) Planetary boundary layer height over the Indian subcontinent during extreme monsoon years. J Atmos Sol Terrest Phys 92:94–99

Pleim JE (2007a) A combined local and nonlocal closure model for the atmospheric boundary layer. part I: model description and testing. J Appl Meteorol Climatol 46:1383–1395

Pleim JE (2007b) A combined local and nonlocal closure model for the atmospheric boundary layer. part II: application and evaluation in a mesoscale meteorological model. J Appl Meteorol Climatol 46:1396–1409

Potty KVJ, Mohanty UC, Raman S (1997) Effect of three different boundary-layer parameterizations in a regional atmospheric models on the simulation of summer monsson circulation. Bound Layer Meteorol 84:363–381

Rajesh PV, Pattnaik S, Rai D et al (2016) Role of land state in a high resolution mesoscale model for simulating the Uttarakhand heavy rainfall event over India. J Earth Syst Sci 125:475–498. https://doi.org/10.1007/s12040-016-0678-x

Roeckner E, Brokopf R, Esch M et al (2006) Sensitivity of simulated climate to horizontal and vertical resolution in the ECHAM5 atmosphere model. J Clim 19:3771–3791

Sandeep A, Rao TN, Ramkiran CN, Rao SVB (2014) Differences in atmospheric boundary-layer characteristics between wet and dry episodes of the Indian summer monsoon. Bound Layer Meteorol 153:217–236

Sathyanadh A, Prabha TV, Balaji B et al (2017a) Evaluation of WRF PBL parameterization schemes against direct observations during a dry event over the Ganges valley. Atmos Res 193:125–141

Sathyanadh A, Prabhakaran T, Patil C, Karipot A (2017b) Planetary boundary layer height over the Indian subcontinent: variability and controls with respect to monsoon. Atmos Res 195:44–61

Sikka DR (1977) Some aspects of the life history, structure, and movement of monsoon depressions. Pure Appl Geophys 115:1501–1529

Singh KS, Bonthu S, Purvaja R et al (2018) Prediction of heavy rainfall over Chennai Metropolitan City, Tamil Nadu, India: impact of microphysical parameterization schemes. Atmos Res 202:219–234

Skamarock WC, Klemp JB, Dudhia J et al (2008) A description of the advanced research WRF Version 3. Technical report NCAR/TN-475 + STR, National Centre for Atmospheric Research, Boulder, Colorado

Srinivas CV, Yesubabu V, Prasad DH et al (2018) Simulation of an extreme heavy rainfall event over Chennai, India using WRF: sensitivity to grid resolution and boundary layer physics. Atmos Res 210:66–82

Strachan J, Vidale PL, Hodges K et al (2013) Investigating global tropical cyclone activity with a hierarchy of AGCMs: the role of model resolution. J Clim 26:133–152

Willmott CJ (1981) On the validation of models. Phys Geogr 2:184–194

Wisse JSP, Arellano VGD (2004) Annales geophysicae analysis of the role of the planetary boundary layer schemes during a severe convective storm. Ann Geophys 22:1861–1874

Zhang D-L, Zheng W-Z (2004) Diurnal cycles of surface winds and temperatures as simulated by five boundary layer parameterizations. J Appl Meteorol 43:157–169

ZiQian W, AnMin D, GuoXiong WU (2014) Impacts of boundary layer parameterization schemes and air-sea coupling on WRF simulation of the East Asian summer monsoon. Sci China Earth Sci 57:1480–1493